LETTER • OPEN ACCESS

Impact of tropical convective conditions on solar irradiance forecasting based on cloud motion vectors

To cite this article: Arindam Roy *et al* 2022 *Environ. Res. Lett.* **17** 104048

View the article online for updates and enhancements.

You may also like

ENVIRONMENTAL RESEARCH
LETTERS

LETTER

Impact of tropical convective conditions on solar irradiance forecasting based on cloud motion vectors

Arindam Roy[1,*] , Annette Hammer[1], Detlev Heinemann[2], Ontje Lünsdorf[1] and Jorge Lezaca[1]

[1] Energy System Analysis, German Aerospace Center (DLR) Institute of Networked Energy Systems, Oldenburg, Germany
[2] Institute of Physics, University of Oldenburg, Oldenburg, Germany
* Author to whom any correspondence should be addressed.

E-mail: arindam.roy@dlr.de

Abstract

Intra-day forecasts of global horizontal solar irradiance (GHI) are widely produced by displacing existing clouds on a geo-stationary satellite image to their future locations with cloud motion vectors (CMVs) derived from preceding images. The CMV estimation methods assume rigid cloud bodies with advective motion, which performs reasonably well in mid-latitudes but can be strained for tropical and sub-tropical climatic zones during prolonged periods of seasonal convection. We study the impact of the South Asian monsoon time convection on the accuracy of CMV based forecasts by analysing 2 years of forecasts from three commonly used CMV methods—Block-match, Farnebäck (Optical flow) and TV-L[1] (Optical flow). Forecasted cloud index (CI) maps of the entire image section are validated against analysis CI maps for the period 2018–2019 for forecast lead times from 0 to 5.5 h. Site-level GHI forecasts are validated against ground measured data from two Baseline Surface Radiation Network stations—Gurgaon (GUR) and Tiruvallur (TIR), located in hot semi-arid and tropical savanna climatic zones respectively. The inter-seasonal variation of forecast accuracy is prominent and a clear link is found between the increase in convection, represented by a decrease in outgoing longwave radiation (OLR), and the decrease in forecast accuracy. The GUR site shows the highest forecast error in the southwest monsoon period and exhibits a steep rise of forecast error with the increase in convection. The highest forecast error occurs in the northeast monsoon period of December in TIR. The impact of convection on the number of erroneous time blocks of predicted photovoltaic production is also studied. Our results provide insights into the contribution of convection to errors in CMV based forecasts and shows that OLR can be used as a feature in future forecasting methods to consider the impact of convection on forecast accuracy.

1. Introduction

Solar photovoltaic (PV) power forecasting is essential for secure and economic injection of the generated electricity into the grid and capturing the cloud-induced output fluctuations is a major challenge in increasing the accuracy of such predictions. As of June 2022, the installed capacity of solar PV systems connected to the Indian electricity grid has reached 57 GW based on the statistics from the Central Electricity Authority of India (https://cea.nic.in/installed-capacity-report/?lang=en). However, the current installed capacity is only 6.5% of the country's

solar potential of 748 GW, estimated by the Ministry of New and Renewable Energy (https://mnre.gov.in/solar/current-status/) while assuming that 3% of the total wasteland area is utilized for solar PV installation.Furthermore, the installed capacity is expected to increase manifolds in the upcoming years in order to fulfil the target of 300 GW of solar generation capacity by 2030 (Malik *et al* 2020, Kumar *et al* 2021). In this regard, the increasing importance of generation forecast has been highlighted in several studies such as in the reports of the Green Energy Corridors (https://mnre.gov.in/img/documents/uploads/80f821f916274ab9b73ac8869a0fa619.pdf) project

under the Indo-German Energy Programme and in the SAARC Energy Centre's report (www.saarcenergy.org/wp-content/uploads/2021/02/Draft-of-Study-Report-on-Assessment-of-wind-and-solar-power-forecasting-techniques-in-SAARC-countries_02.12.2020.pdf). Short-term forecasting and scheduling of solar energy generation has become a widely pursued area of research and policy development in the Indian context due to the challenges involved in the large-scale integration of solar PV into the existing grid (Das 2017). The Indian Central Electricity Regulatory Commission (CERC, https://cercind.gov.in/2015/regulation/SOR7.pdf) and the other state regulators (www.tnerc.gov.in/Regulation/files/Reg-120220211048Eng.pdf) set deviation margins (e.g. 10% of the nominal capacity) for fluctuating renewable generation systems like solar PV within their area. Deviations are calculated for each 15 min time block. This has financial implications for the operators of large-scale solar PV systems in terms of crossing deviation penalty margins. CERC regulation allows for a fixed number of intra-day revisions to the day-ahead schedule of solar PV generators up to 1.5 h before the delivery time. In such a situation, choosing the less erroneous forecast can make a significant difference. Deviation of solar PV generation from the day-ahead forecasted schedule across a large region causes load-generation imbalance in the power system and hampers the frequency stability. Short-term deviations of renewable generation from their forecasts in this time period require balancing capacities in terms of reserves. Due to the intermittency of solar PV and wind generators, power system operators in India sometimes need to perform emergency curtailment of solar PV and wind generation to maintain the grid stability. This not only causes financial losses for these generators, but also leads to a wastage of emission-free renewable energy. Clouds are the main source of uncertainty in hours-ahead PV power forecast and their effects can be captured by satellite-based methods to a large extent. Geostationary satellite images can provide information at spatio-temporal resolution appropriate for cloud detection and cloud motion estimation.

Deep convective systems present complex cloud situations which involve motion in all three dimensions along with growth and decay. The South Asian monsoon occurs over a span of a few months during which there are frequent occurrences of deep convective systems. It is caused by the northward and southward propagation of the Inter-Tropical Convergence Zone (ITCZ) from the equator, in response to the seasonal variation of the latitude of maximum insolation (Gadgil 2003, Sharma *et al* 2021). This leads to the formation of two distinct monsoon patterns—the southwest or summer monsoon (June to September) and the northeast or winter monsoon (October to December), during the northward and the southward shift of the ITCZ respectively.

During the summer monsoon, the ITCZ advances northward over the Indian Ocean into the subcontinent (20°–25° N) from its near-equatorial position (Sikka *et al* 1986). The intense solar heating through boreal spring and summer, and the difference in heat capacity between the South Asian landmass and the adjoining oceans leads to the development of a large-scale meridional surface temperature gradient (Turner and Annamalai 2012). The withdrawal of the summer monsoon and the onset of the winter monsoon is characterized by the reversal of lower level wind direction from southwest to northeast (Rajeevan *et al* 2012). The ITCZ retreats towards its near-equatorial position during the winter monsoon with the maximum cloudiness observed over the southern peninsular part (Wonsick *et al* 2009). The monsoon period in general is characterized by frequent formation and dissipation of convective clouds over the landmass.

Motion extraction techniques were originally used in video compression for removing redundancy from consecutive frames in order to reduce the total size (Cros *et al* 2014). Global solar horizontal irradiance (GHI) forecasts for future time instances are obtained by extrapolating cloud structures forward in time with the cloud motion vectors (CMVs) estimated from past consecutive images, considering clouds as rigid bodies with purely advective motion. Various CMV techniques are already used commercially, and several others are available in literature (Hammer *et al* 1999, Lorenz *et al* 2004, Lee *et al* 2017, Gallucci *et al* 2018). Block-matching is the most widely used operational CMV estimation method from geostationary images (Cros *et al* 2014a, Hammer *et al* 1999). It estimates the CMVs by calculating the spatial correlation between nearby blocks in consecutive images. Optical flow (OF) techniques emerged from research in the field of computer vision, for object detection and tracking (Bai and Huang 2018, Oh *et al* 2021). They involve the use of differential techniques for estimating the apparent motion of image objects between two sequential frames caused by either the movement of the object or the camera (Urbich *et al* 2018, 2019, Li *et al* 2019). Urbich *et al* (2018) compared the performances of Farnebäck and TV-L^1 OF methods in forecasting cloud albedo for 10 exemplary days and found that TV-L^1 performed the best. André *et al* (2019) validated the performances of block-match, spatio-temporal autoregressive and scaled persistence methods in producing intra-day GHI forecasts for the Guadeloupe island over a period of 2 years with satellite images. Kallio-Myers *et al* (2020) applied Farnebäck technique to produce site-level GHI forecasts, and validated them against ground measurements from five sites in Finland for a period of 4 months. Smart persistence of satellite images was used as the reference to highlight the superior accuracy of Farnebäck. Al-Amaren *et al* (2021) used framewise

peak signal-to-noise ratio (PSNR) to validate the accuracy of motion vectors in video compression. Cros *et al* (2020) produced intraday GHI forecasts by applying the block-match method on satellite images and validated them against the ground measured irradiance from the Palaiseau Baseline Surface Radiation Network (BSRN) site for a period of 3 years covering different weather regimes. Oh *et al* (2021) performed a spatial analysis of the performance of several OF and deep learning based CMV extraction methods over the South Korean peninsula with 1 year of satellite images.

Several authors implemented and validated forecasting methods for the different satellites around the globe. Prasad and Kay (2021) benchmarked solar power forecasts with Himawari-8 images against four sites in Australia for 1 month. The authors used the Farnebäck method for CMV estimation with Heliosat for converting pixel intensity to solar irradiance and found that the site located in arid climatic zone had the highest forecast error. Notable errors were reportedly due to changes in image contrast in situations involving rapidly developing cumulus congestus clouds. Kim *et al* (2017) estimated GHI over the Korean Peninsula and a part of the Japanese islands from COMS images using the UASIBS/KIER model, which takes visible channel reflectance and infrared channel brightness temperatures as inputs. Yang *et al* (2019) presented a model for forecasting GHI up to 3 h ahead with visible and infrared channel images from the Fengyun-4 satellite and its validation against measurements from a site in the Gobi Desert for some sample days. The authors used particle image velocimetry (PIV) for estimating the motion field and a cloud/shadow detection algorithm (Zhai *et al* 2018) based on spectral indices for deriving GHI from satellite reflectivity values. Yang *et al* (2020) used the Heliosat 2 and the PIV method for estimating GHI and the motion field respectively. They validated the forecasts against ground measurements from a site for a few typical months. They found that the forecasts perform best in January and the worst in July for the Chengde site. Cheung *et al* (2015) analysed the spatio-temporal variation in cloud cover and the resulting reduction in surface solar irradiance at eight sites distributed across Australia. Mejia *et al* (2018) assessed the seasonal day-ahead GHI forecast accuracy of numerical weather prediction (NWP) data from the weather and research forecasting (WRF) model against ground measurements from a site in Las Vegas, Nevada for the period August 2015 to December 2016. Similar studies on the seasonal variability of NWP based day-ahead irradiance forecast for different regions can be found in the literature (Lara-Fanego *et al* 2012, Ohtake *et al* 2013, 2015). Gregory *et al* (2012) cited incorrect representation of convective clouds in the tropics and orographic lifting over mountainous areas in southeastern Australia as the primary causes behind day-ahead GHI forecast

error. Huang *et al* (2018) performed a climatological validation and inter comparison of multiple NWP models over the entire Australian landmass with 1 year of data. They found a strong correlation between the monthly forecast error and monthly cloudiness by validation against ground measured data from 13 sites. Tuononen *et al* (2019) investigated how operational NWP forecasts of low and mid-level clouds affect the accuracy of GHI forecasts with 4 years of cloud and GHI observations from a site in Helsinki, Finland. They observed that the relative error in solar irradiance forecast remains more or less constant throughout the year.

The aforementioned CMV based forecast methods have primarily been tested for mid-latitude climatic zones with predominantly advective cloud motion. Wonsick *et al* (2009) extensively studied the seasonal variation of the total cloud cover at various locations inside the Indian monsoon region with images from Meteosat-5. However, the relation between cloud cover and GHI forecast accuracy has not been analysed. In Mao and Wu (2007) and Yamazaki and Nakamura (2021), the authors utilized satellite estimated outgoing longwave radiation (OLR) as a measure of convection. Aicardi *et al* (2022) benchmarked the performance of block-match and three other OF techniques with a 1 year dataset of GOES-East satellite images of a region in south-east South America. The authors found that TV-L^1 performed the best on an average, but concluded that further studies into the relation between regional cloudiness regime and CMV performance are required for different parts of the globe. A brief overview of the relevant studies have been provided in table 1. Under the convection dominated weather situation in the tropics, the underlying assumptions for CMV estimation may not be adhered to. For an individual solar PV system, this would imply an increase in erroneous forecast updates and intra-day bids at the power exchange. With many such systems connected to the grid, the deviation of the actual generation from the forecasted could pose significant load-generation balance problems for the grid operator. Additionally, the intra-annual or seasonal variability in this forecast error may affect long-term planning and the optimal location of solar PV systems (Davy and Troccoli 2011). In particular, a performance analysis of the CMV methods for duration long enough to capture the seasonal effects in tropical climatic regions, is missing. In this paper, the performance of the operational Block-match technique and two other commonly used OF methods—Farnebäck and TV-L^1, are analysed for a period of 2 years (2018–2019) and the following contributions made:

- Quantification of the impact of seasonal convection on CMV based solar irradiance forecast accuracy in two Köppen-Geiger climatic zones.

Table 1. Review of recent satellite derived solar irradiance methods for different regions around the globe, as well as studies considering seasonal forecast accuracy, impact of cloudiness or convection.

Author	Region	Source	Method	Horizon	Convection studied
Yang *et al* (2019)	Gobi Desert	Fengyun-4	Particle image velocimetry (PIV)	3 h	No
Aicardi *et al* (2022)	South America	Geostationary Operational Environmental Satellite (GOES) East	Block-match and several OF methods	5 h	Indirectly
Prasad and Kay (2021)	Australia	Himawari 8	Farnebäck	5 min/15–25 min	No
Huang *et al* (2018)	Australia	Global Forecasting System (GFS), European Centre for Medium-Range Weather Forecasts (ECMWF), Australian Community Climate and Earth-System Simulator (ACCESS)	NWP	6 h/12 h	Indirectly
Kim *et al* (2017)	Korean Peninsula	Communication, Ocean and Meteorological Satellite (COMS)	No forecasting performed	—	No
Wonsick *et al* (2009)	Indian subcontinent	Meteosat 5	No forecasting performed	—	Yes
Mao and Wu (2007)	Eastern Bay of Bengal	National Centers for Environmental Prediction-National Center for Atmospheric Research (NCEP-NCAR) reanalysis product, National Oceanic and Atmospheric Administration (NOAA) Outgoing longwave radiation (OLR) product	OLR as a measure of convection, no forecasting performed	—	Yes
Yamazaki and Nakamura (2021)	Tropical Indian Ocean	ECMWF reanalysis (ERA) interim product, NOAA OLR product	OLR as a measure of convection, no forecasting performed	—	Yes
Tuononen *et al* (2019)	Finland	ECMWF	NWP	24–48 h	No

- Analysis of the variation of forecast error with change in OLR, used as a proxy for convection.
- Seasonal comparison of the accuracy of the block-match, OF and persistence methods for solar PV power prediction in terms of erroneous 15 min time-blocks.

2. Data and method

2.1. Data

2.1.1. Satellite images
Data from the Meteosat Second Generation-Indian Ocean Data Coverage (MSG-IODC) is used for deriving cloud information, which is available from the EUMETSAT archive (https://archive.eumetsat.int/). Meteosat-8, centred at 41.5° E, provides the MSG-IODC service since February 2017 (Bushair *et al* 2021). The Spinning Enhanced Visible and InfraRed Imager aboard MSG satellites observe the Earth in 12 channels covering the visible, near-infrared and infrared spectral range (Hutt *et al* 2020). In the visible range, the radiances registered by the imager are dominated by sun-scattered photons and do not include the effect of the Earth surface or cloud-top emissions (Geiss *et al* 2021). Furthermore, the error in albedo at 0.6 μm is less than that at 0.8 μm. In this analysis, visible channel data centred at 0.6 μm with a spatial resolution of 3 km $\times$ 3 km at nadir is utilized for the time period 01-2018 to 12-2019.

2.1.2. Ground measurements
Ground measured GHI data available at 1 min temporal resolution from two stations of the World Meteorological Organization's BSRN (Kumar *et al* 2014, Driemel *et al* 2018) in India namely—Gurgaon (GUR) and Tiruvallur (TIR) are used for the validation of the satellite predicted GHI. The GUR BSRN site, located in northern India (28.42° N 77.16° E),

Figure 1. Monthly averaged OLR for (a) the summer monsoon period of August and (b) the winter monsoon period of December (data source: Liebmann and Smith 1996).
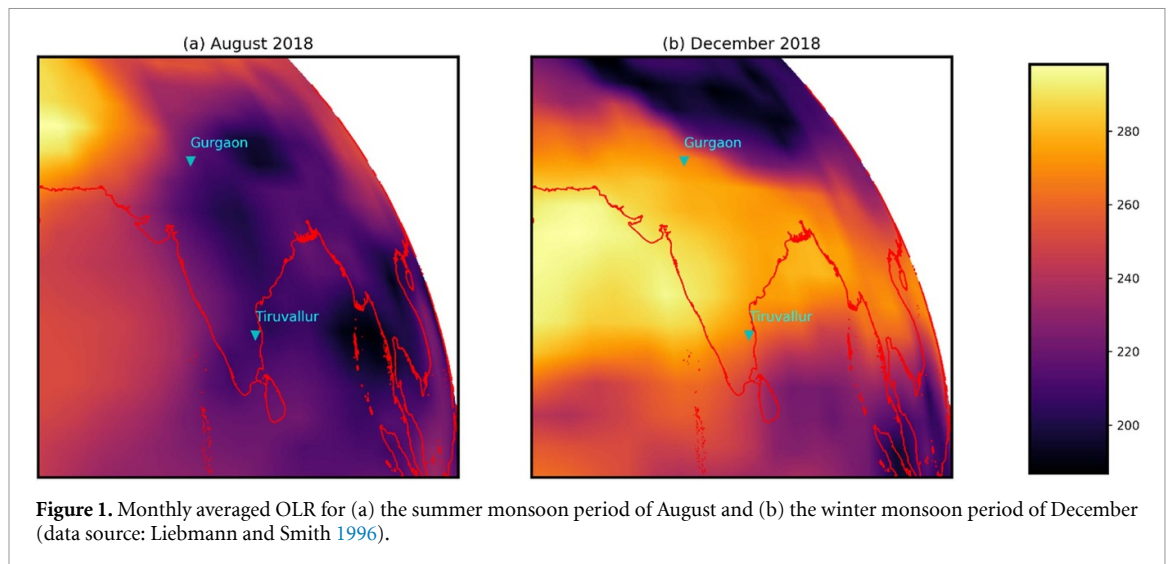
is affected by the summer monsoon and falls under the hot semi-arid climatic zone (BSh) defined by Köppen-Geiger classification (Beck *et al* 2018). The TIR BSRN site on the other hand is located in Southern India (13.09° N 79.97° E) and is affected by the winter monsoon. It falls under the tropical savanna type (Aw) of climatic zone.

2.1.3. OLR

Monthly averaged and daily averaged OLR data from the climate prediction centre of the National Center for Environmental Prediction is used as a measure of convection. The OLR dataset is derived using a multi-spectral technique involving the water vapour channel and multiple infrared channels. So, it can detect convection with higher certainty than the brightness temperature from any single infrared channel. It has a spatial resolution of 2.5° latitude × 2.5° longitude and a spatial coverage of 90.0° N–90.0° S, 0.0° E–357.5° E (Liebmann and Smith 1996). It is derived from the NOAA 18 polar orbiting satellite images available from September 2005 till the present time and has a daily temporal resolution. The low spatial resolution causes convective activities in the wider vicinity to be considered when analysing the OLR at any point. This is appropriate for the present study due to the forecast horizon of 5 h. Since we study the effect of seasonal convection on the irradiance forecast accuracy, the daily temporal resolution is found to be sufficient. Figure 1 shows the OLR map constructed from this data for the South Asian section over the summer and winter monsoon periods of 2018. In Ghanekar *et al* (2010), Jiang and Zhu (2020) and Su *et al* (2020), an OLR value of less than 250 W m^{-2} is considered as an indication of tropical convection while a value less than 240 W m^{-2} signifies deep convection. As noted in Midhuna and Dimri (2019), OLR is influenced by the presence of convective clouds and cold surface earth temperature as well.

Therefore, a careful interpretation of the OLR over the Himalaya is necessary.

2.2. Methods

2.2.1. Pre-processing satellite image

The original MSG-IODC high rate information transmission (HRIT) image has a size of 3712 pixels × 3712 pixels and covers large parts of Africa and Asia. This image is cropped to a size of 1200 pixels × 1200 pixels to fit the South Asian section, as shown in figure 2(a). Enough margin is allocated to be able to detect incoming clouds in advance. The section extends from 1.39° N to 43.34° N and 58.04° E to 122.27° E. The digital counts from the satellite image are converted to radiances with the calibration factors given in the image headers. They are further converted to bidirectional reflectance factors (BRFs) according to the EUMETSAT report for the conversion of radiance to reflectance (www-cdn.eumetsat.int/files/2020-04/pdf_msg_seviri_rad2refl.pdf). From these cloud index (CI) images are processed using the Heliosat method (Hammer *et al* 2015). The CI is a measure of cloudiness, as shown in figure 2(b). It is defined as shown in equation (1)

$$CI = \frac{\rho - \rho_0}{\rho_c - \rho_0}. \tag{1}$$

ρ is the actual BRF value of a given pixel. ρ_0 and ρ_c are determined using a time series of BRFs. ρ_0 is estimated individually for each pixel and is assumed to be the most frequent low value (5th percentile) of reflectance in the time series of a given pixel. ρ_c, on the other side, is estimated for the entire image and corresponds to the most frequent high value of reflectance (95th percentile of all values of $\rho > 0.5$) in the time series considering all pixels. Both values are daily updated using images of the same time for the previous 30 d.

Figure 2. (a) South Asian section with visible channel centred at 0.6 μm from Meteosat-8 on 31 March 2019 08:00 UTC ©EUMETSAT and (b) the resulting cloud index information.
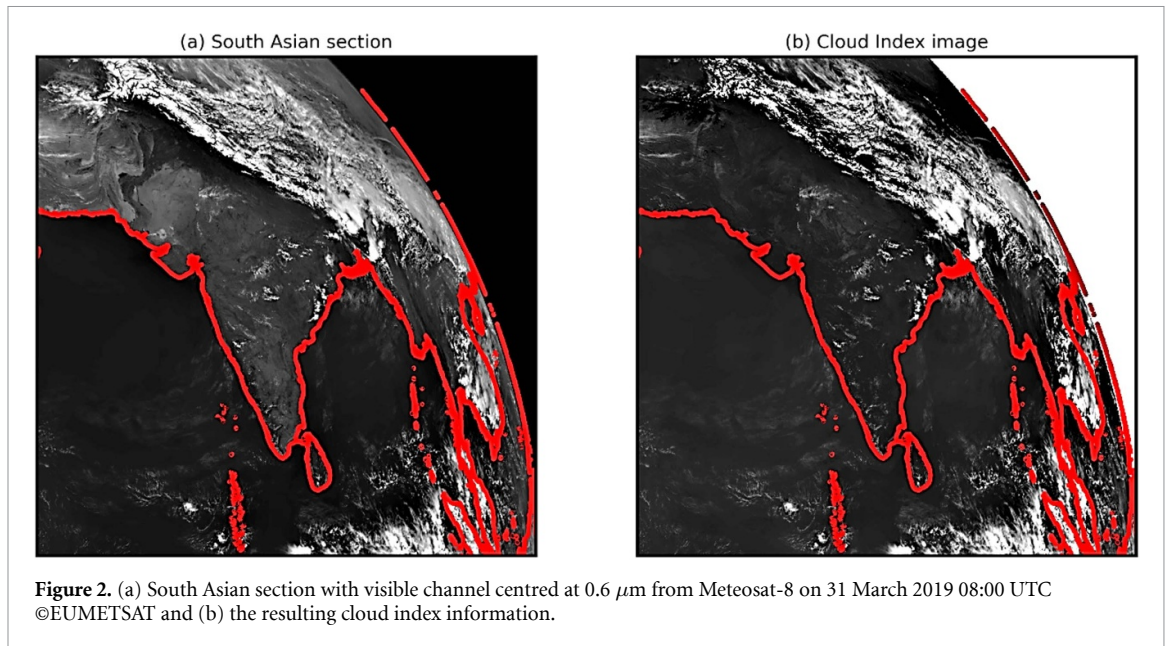
The final step of the Heliosat method is to transform CI to GHI as described in Hammer *et al* (2015). For this, the clear sky model introduced in Dumortier (1995) with climatological turbidity values from an International Energy Agency (IEA) report by Remund and Domeisen (https://meteonorm.com/assets/publications/ieashc36_report_TL_AOD_climatologies.pdf) are used. Forecasts of GHI are produced by applying this last step of the Heliosat method on forecasted CI images and using the expected clear sky irradiance for the time ahead.

2.2.2. CMV estimation techniques

Although different in their implementation, the various CMV methods make similar basic assumptions:

- Cloud pixel intensity values remain constant along motion trajectories.
- Cloud motion is advective and there is no formation or dissipation of clouds between consecutive images.
- CMV fields are smooth over a window or block.

The block-match technique (Lorenz *et al* 2004, Gallucci *et al* 2018) looks for the best matching image segment or block in terms of the least mean squared error between two consecutive images and within a search window to estimate the displacement of cloud structures. The operational block-match algorithm used at the German Aerospace Center (DLR, Institute of Networked Energy Systems) on Meteosat-10 derived CI images, is tuned for the South Asian section. We tested the sensitivity of the Blockmatch algorithm for different block (21, 26, 31, 36, 41, 46) and search window sizes (37, 42, 47, 52, 57, 62). A block size of 31 pixels ($\approx$31 $\times$ 3 km = 93 km at Nadir) and a search window of ($\approx$47 $\times$ 3 km = 141 km at

Nadir) shows the best results. In Aicardi *et al* (2022), the authors found 120 and 144 pixels as the optimum values of block and search window sizes for 1 km resolution GOES East image section of south-east South America.

OF employs differential methods to extract motion vectors for small displacements and uses a pyramidal approach to detect large displacements (Bai and Huang 2018, Li *et al* 2019). The OpenCV (http://opencv.org/) implementation of Farnebäck (Pérez *et al* 2013) and TV-L[1] (Zach *et al* 2007) are used in this analysis. With a similar tuning approach, we found that a window size of 8 pixels ($\approx$24 km at Nadir) is optimum for Farnebäck. This is also comparable to the value of 22 pixels window size at 1 km resolution found optimum in Aicardi *et al* (2022). Furthermore, the authors showed that optimizing the parameters led to a maximum improvement of 2%–3% for Farnebäck and less than 1% for TV-L[1]. The time step parameter of TV-L[1] is kept the same as in Urbich *et al* (2018) at 0.1. Tables 2 and 3 show the complete list of parameters used in Farnebäck and TV-L[1].

We chose images with a time difference of 30 min due to the low spatial resolution of 3 km $\times$ 3 km. Using a higher temporal resolution is not necessary due to the effect of the spatial resolution on slow moving clouds like cumulus. In Yang *et al* (2020), the authors also chose a temporal resolution of 30 min when analysing irradiance forecasts from a channel of 2 km $\times$ 2 km spatial resolution. The CMV fields estimated by the three different methods are visualized in figure 3 for one example pair of images from 14 June 2019 07:00 UTC and 14 June 2019 06:30 UTC images. The direction of motion and the magnitude of motion are indicated by colour and intensity of the colour, respectively. It can be observed that the direction of rotation of the cyclonic formation

Table 2. Parameters of OpenCV Farnebäck implementation.

Parameter	Value	Description
Flow	None	Initial approximation of flow
Pyr_scale	0.5	Scaling factor of the image pyramid (<1)
Levels	3	Number of pyramid levels
Winsize	8	Averaging window size
Iterations	3	Number of iterations at each pyramid level
Poly_n	7	Size of the pixel neighbourhood for polynomial expansion
Poly_sigma	1.5	Standard deviation of the Gaussian smoothing used in the polynomial expansion
Flags	false	OPTFLOW_USE_INITIAL_FLOW: to use an initial flow approximation
		OPTFLOW_FARNEBACK_GAUSSIAN: to use a Gaussian filter inside the averaging window

Table 3. Parameters of OpenCV TV-L^1 implementation.

Parameter	Value	Description
Time step (τ)	0.1	Time step of the numerical scheme for convergence
Attachment parameter (λ)	0.03	Weights between the data fidelity and the regularization term. Determines the smoothness of the output.
Tightness parameter (θ)	0.3	Links the attachment and the regularization terms
Scales (N_{scales})	3	Number of pyramid levels
Warps (N_{warps})	3	Number of warping operations at each pyramid level
Epsilon (ε)	0.01	Stopping criterion
Inneriterations	10	
Outeriterations	2	
Scalestep	0.5	Scaling factor of the image pyramid
Gamma	0.1	Illumination term
Medianfiltering	5	Size of the median filter
Useinitialflow	false	To input an initial approximation of the flow

fits well with the general counter-clockwise motion of cyclones in the northern hemisphere in all the three methods. Block-match detects more areas with motion due to its coarse resolution. TV-L^1 provides the smoothest motion field output. It takes 3.5, 0.4 and 0.1 s respectively for TV-L^1, Farnebäck and block-match to compute the CMV field from an image pair used in this analysis.

2.2.3. Extrapolation of CI image with CMV
The 30 min ahead location of the pixels in the CI image is determined by adding the displacement vectors for each pixel obtained from the CMV estimation method to the row and column numbers of that pixel. These represent the new (row, column) locations of the pixels. Gridded interpolation is then applied to resample the CI pixel values in the new grid to the original (row, column) grid. The forecast for 60 min ahead is obtained by displacing the 30 min ahead forecast again by 30 min with the same displacement vectors. The same procedure is repeatedly applied for producing forecasts up to a horizon of 5.5 h.

2.2.4. Conversion of GHI to solar PV power output
In the first step, GHI is split into diffuse horizontal irradiance (DHI) and direct normal irradiance using the Engerer2 model implemented in Bright and Engerer (2019). The module tilts at the

two sites are assumed to be equal to the latitude at the two sites. At both the sites, an installed capacity of 100 MW$_{\text{p}}$ is assumed. DHI is transformed into diffuse tilted irradiance (DTI) using the model introduced in Perez *et al* (1990) and implemented in pvlib (https://pvlib-python.readthedocs.io/en/stable/reference/generated/pvlib.irradiance.perez.html). The global tilted irradiance (GTI) is then obtained by adding the DTI, the direct beam component and the ground reflected component using the pvlib function (https://pvlib-python.readthedocs.io/en/v0.6.0/generated/pvlib.irradiance.get_total_irradiance.html). GTI is converted to DC power with the PVWatts model from pvlib (https://pvlib-python.readthedocs.io/en/v0.4.2/generated/pvlib.pvsystem.pvwatts_dc.html) assuming that there is no effect of temperature or wind speed on module power output, as shown in equation (2). The inverter AC power output is estimated using the PVWatts inverter model (https://pvlib-python.readthedocs.io/en/stable/reference/generated/pvlib.inverter.pvwatts.html) as shown in equation (3). The inverters are assumed to have a nominal efficiency of 96% and a reference efficiency of 96.37%. ζ is the ratio of the actual DC power input and the DC power input limit of the inverter

$$\text{Power}_{\text{DC}} = \frac{\text{GTI}}{1000} \times \text{MW}_{\text{p}} \qquad (2)$$
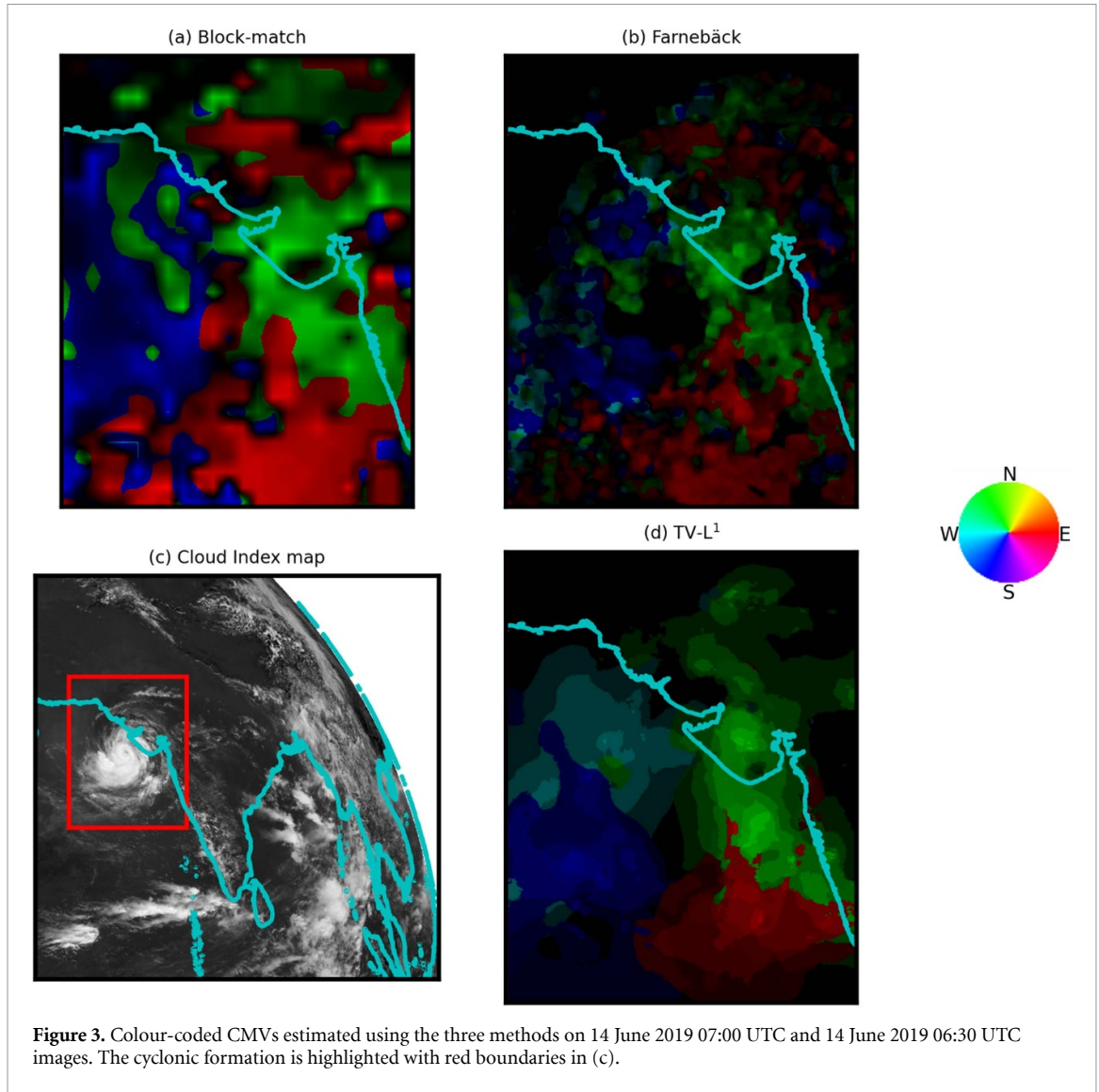
Figure 3. Colour-coded CMVs estimated using the three methods on 14 June 2019 07:00 UTC and 14 June 2019 06:30 UTC images. The cyclonic formation is highlighted with red boundaries in (c).

$$\eta = \frac{\eta_{\text{nom}}}{\eta_{\text{ref}}} \left(-0.0162\zeta - \frac{0.0059}{\zeta} + 0.9858 \right). \quad (3)$$

2.2.5. Forecast evaluation technique

The satellite-based forecasts from all the four methods (CI persistence as reference, and three CMV approaches) are validated at the section-wide level and at the two BSRN sites over the daytime period for a forecast horizon of 0–330 min ahead with 30 min forecast steps (see figures 4(a)–(c), 5(a)–(c), 7(a)–(c) and 8(a)–(c)). The forecasted CI maps for the entire section are validated against the real-time analysis CI maps for the period 2018–2019 using the PSNR metric shown in equation (7). PSNR is the ratio of the maximum possible value of an $m \times n$ image or signal MAX_f (here 1) to the magnitude of distorting noise or error $\text{RMSE}_{\text{section}}$ and is expressed in decibels (dBs) (Poobathy and Chezian 2014). $\text{PSNR}_{\text{section}}^{x\,\text{minutes}}$ values are computed separately for each forecast horizon from 0 to 330 min ahead. A higher value of PSNR implies a better match between the predicted and the analysis image

$$\text{RMSE}_{\text{site}} = \sqrt{\frac{1}{N}\sum_{n=1}^{N}\left(\text{GHI}_{\text{pred}} - \text{GHI}_{\text{meas}}\right)^2} \quad (4)$$

$$\text{MAE}_{\text{site}} = \frac{1}{N}\sum_{n=1}^{N}\left|\text{GHI}_{\text{pred}} - \text{GHI}_{\text{meas}}\right| \quad (5)$$

$\text{RMSE}_{\text{section}}$

$$= \sqrt{\frac{1}{m \times n}\sum_{i=0}^{m-1}\sum_{j=0}^{n-1}\left|f_{\text{pred}}\left(i,j\right) - f_{\text{analys}}\left(i,j\right)\right|^2} \quad (6)$$

$$\text{PSNR}_{\text{section}}^{x\,\text{minutes}} = 20\log_{10}\left(\frac{\text{MAX}_f}{\text{RMSE}_{\text{section}}^{x\,\text{minutes}}}\right). \quad (7)$$

Site-level CI forecasts for the co-ordinates of the two BSRN stations are extracted from the forecasted CI maps for the calendar year 2018 and transformed to irradiance as described in section 2.2.1. The GHI forecasts are validated against ground measurements using the root mean square error metric as shown in equation (4). The $\text{RMSE}_{\text{site}}$ values are normalized
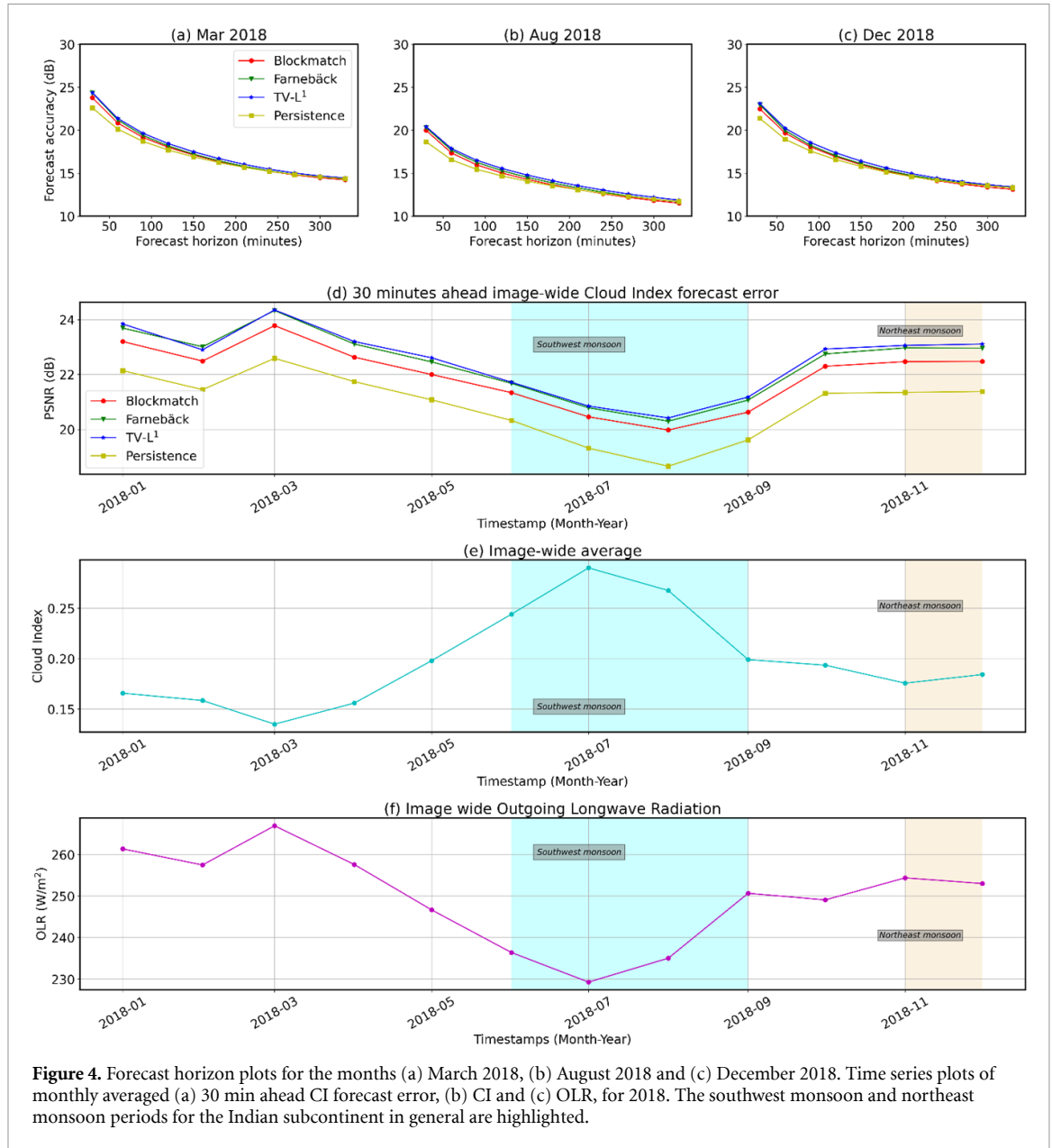
Figure 4. Forecast horizon plots for the months (a) March 2018, (b) August 2018 and (c) December 2018. Time series plots of monthly averaged (a) 30 min ahead CI forecast error, (b) CI and (c) OLR, for 2018. The southwest monsoon and northeast monsoon periods for the Indian subcontinent in general are highlighted.

by the average non-zero ground measured GHI computed separately for each forecast step ahead from 30 to 330 min (see equation (8)) to obtain the normalised root mean square error (nRMSE). The normalised mean absolute error (nMAE) is calculated as shown in equation (9).

$$nRMSE_{site}^{x\,minutes} = \frac{RMSE_{site}^{x\,minutes}}{\left(\frac{\sum_{n=1}^{N} GHI_{meas}^{x\,minutes}}{N}\right)} \times 100 \quad (8)$$

$$nMAE_{site} = \frac{MAE_{site}^{x\,minutes}}{\left(\frac{\sum_{n=1}^{N} GHI_{meas}^{x\,minutes}}{N}\right)} \times 100. \quad (9)$$

Additionally, a no cloud motion or persistence of CI map forecast is also considered in this analysis as the worst-case reference. The same analysis CI map is assumed to persist up to 330 min ahead.

The PV power forecast error is calculated according to CERC regulations as shown in equation (10) (https://cercind.gov.in/2015/regulation/SOR7.pdf)

$$Error_{PV}$$
$$= \frac{|ScheduledGeneration - ActualGeneration| \times 100}{AvailableCapacity}.$$
$$(10)$$

3. Results

3.1. Validation against reference analysis maps
It is expected, that the forecast accuracy drops from an initial high value and gets more and more inaccurate with increasing forecast horizon. This is illustrated in figures 4(a)–(c) and 5(a)–(c). The section-wide CI forecast accuracy is presented for the months of March, August and December with high, low and intermediate values of observed accuracy respectively. Especially for the short horizons up to 90 min, the
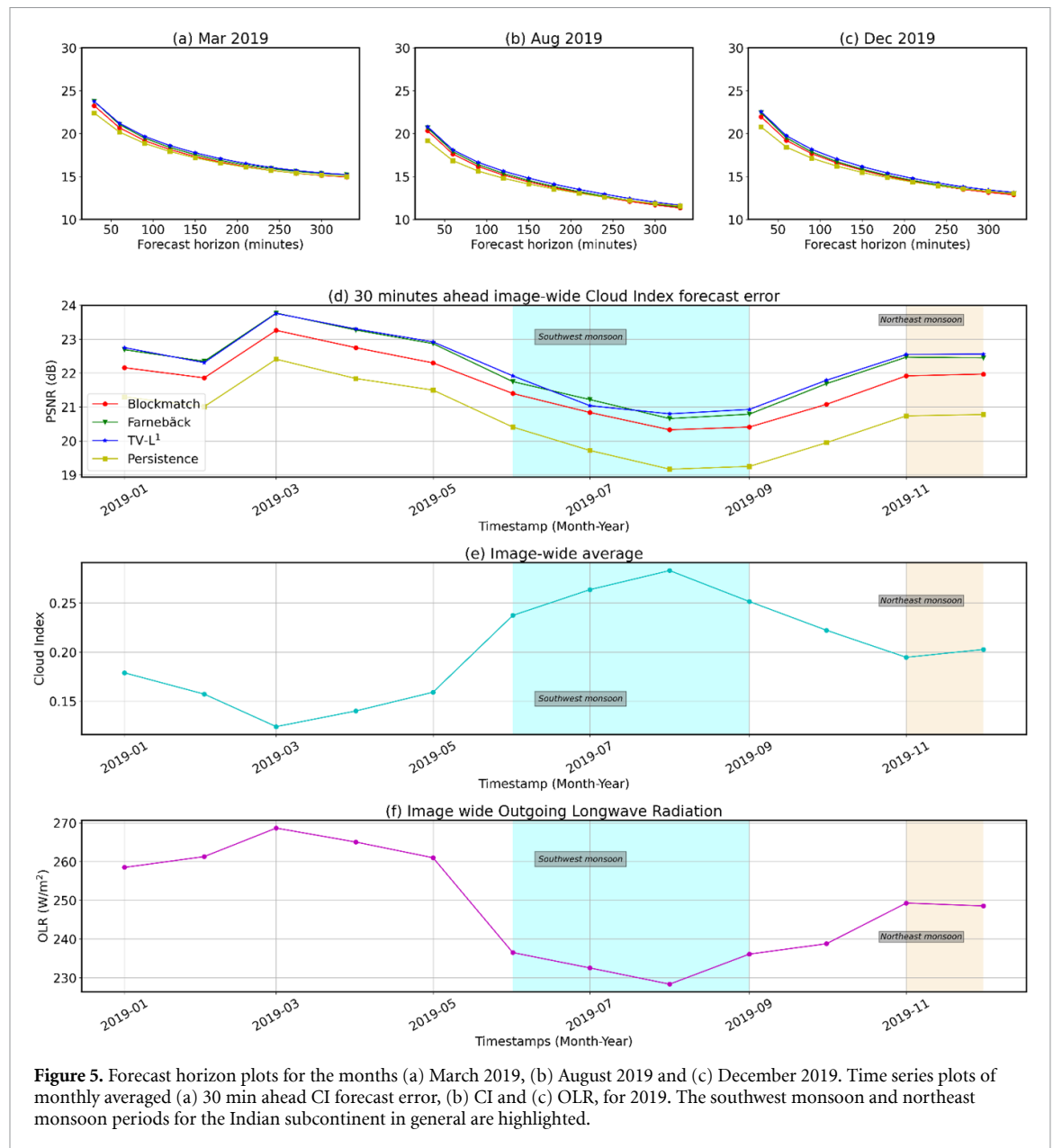
Figure 5. Forecast horizon plots for the months (a) March 2019, (b) August 2019 and (c) December 2019. Time series plots of monthly averaged (a) 30 min ahead CI forecast error, (b) CI and (c) OLR, for 2019. The southwest monsoon and northeast monsoon periods for the Indian subcontinent in general are highlighted.

Table 4. Average performance of the 30 min ahead section-wide CI forecasts for 2018–2019.

Method	PSNR (dB)
Blockmatch	21.80
Farnebäck	22.26
TV-L^1	22.33
Persistence	20.75

CMV methods outperform the persistence method. The worst performance is observed in August, where the PSNR drops below 15 dB for forecast horizons longer than 120 min for all methods.

On an average, TV-L^1 outperforms all the other methods at the section-wide level as seen in table 4, where the 30 min ahead PSNR value is given as the initial best value.

The highest forecast accuracy of 24.35 dB and 23.76 dB for TV-L^1 is observed in the month of March in both 2018 and 2019 respectively as shown in figures 4(d) and 5(d) respectively. During this period, the section-wide average CI is low (<0.15) and the OLR is high (>260 W m^{-2}). Low forecast accuracy for the entire section is observed during the southwest monsoon period of June to September (see table 5) in 2018 and again in 2019 with the lowest— 20.42 dB and 20.80 dB respectively for TV-L^1, occurring in August. High values of section-wide averaged CI (>0.2) are also observed during the southwest monsoon period as shown in figures 4(e) and 5(e). The section-wide averaged OLR remains close to or below 250 W m^{-2} during this period as shown in figures 4(f) and 5(f). Intermediate accuracy values of 23.11 dB and 22.56 dB are observed in December 2018 and 2019 respectively, which is in the northeast monsoon period (see table 5). Both the CI and OLR are found to remain close to the threshold values of 0.2 and 250 W m^{-2} respectively, during this period.

Table 5. Duration of the monsoon period during 2018–2019 as reported by the India Meteorological Department (IMD, www.imdpune. gov.in/Clim_Pred_LRF_New/Reports/Monsoon_Report/monsoon_report_2018.pdf, https://mausam.imd.gov.in/chennai/mcdata/ne_ monsoon_2018.pdf, https://mausam.imd.gov.in/chennai/mcdata/sw_monsoon_2019.pdf, https://mausam.imd.gov.in/chennai/mcdata/ ne_monsoon_2019.pdf, https://reliefweb.int/attachments/87b8bb57-8593-3c9f-a5a6-cd87487974ea/20181102_pr_351.pdf).

Geographic area	Southwest monsoon	Northeast monsoon
Indian subcontinent	June–September	November–December
Gurgaon	July–September	Not observed
Tiruvallur	June–September	November–December
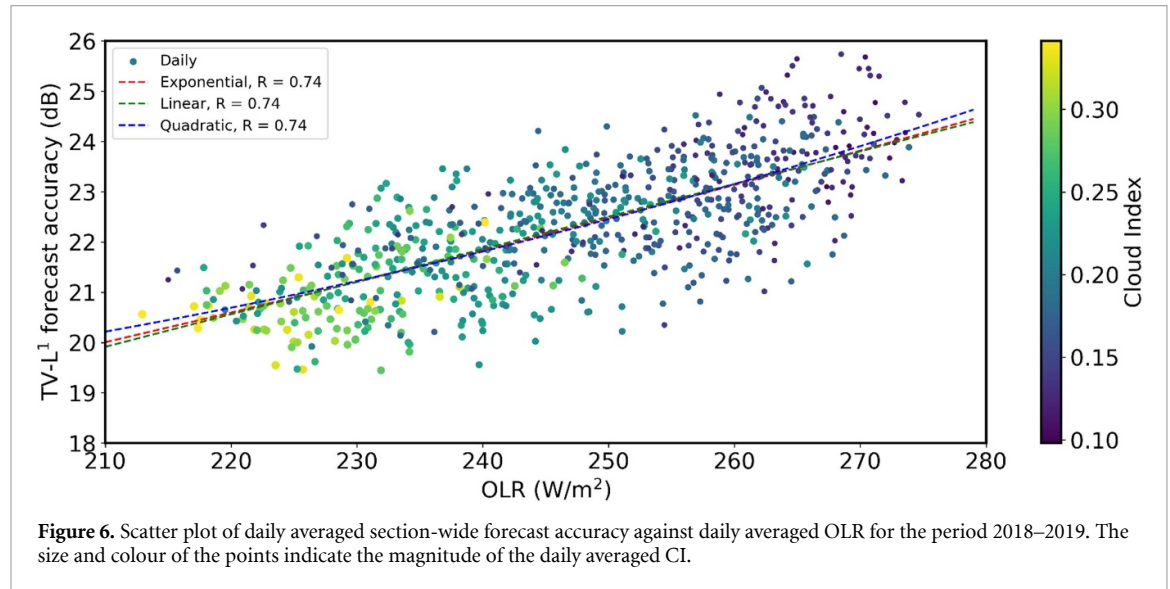
Figure 6. Scatter plot of daily averaged section-wide forecast accuracy against daily averaged OLR for the period 2018–2019. The size and colour of the points indicate the magnitude of the daily averaged CI.

The impact of convection and cloudiness on forecasting accuracy is further analysed with a day to day performance. Figure 6 shows that the forecast accuracy increases with the increase in daily averaged OLR. Low forecast accuracy is typically also observed for the days with high section-wide CI.

3.2. Validation against ground measurements

The variation in forecast error with the forecast horizon for the three selected months is shown in figures 7(a)–(c) for the GUR site and figures 8(a)–(c) for the TIR site. As shown in figure 7(d), the lowest forecast nRMSE is observed at the GUR site in March (9.35% for TV-L[1]). The OLR at the site is also high (>280 W m^{-2}) during this period as seen in figure 7(e). During the July to September southwest monsoon period (see table 5) of 2018 at the GUR site, a high forecast nRMSE is observed. Monthly averaged OLR of less than 230 W m^{-2}, indicative of deep tropical convection, is also observed in the months of July and August 2018 at the GUR site during this period. The highest forecast nRMSE for the CMV based methods is observed in July (29.46% for TV-L[1]). Persistence shows the highest forecast error in August (32.41%), when the OLR at the site is also the least (220 W m^{-2}). Relatively low forecast nRMSE (12.37% for TV-L[1]) and high OLR (270 W m^{-2}) is observed again in December. There is a steep rise in GHI forecast nRMSE at the GUR site with the

decrease in OLR below 250 W m^{-2} as shown in figure 9(a). The *p*-value is close to 0 and implies that the correlation is significant. High CI (>0.4 W m^{-2}) is predominantly observed when the OLR is below 250 W m^{-2}. The quadratic polynomial fit shows the best correlation at 0.7, see figure 10(a).

The averaged 30 min ahead GHI forecast error at the TIR site for each month of the calendar year 2018, is shown in figure 8(d). It must be noted here that ground measured GHI from the TIR station is unavailable due to missing or bad quality data for October and November 2018. The lowest forecast nRMSE of 9.47% (for TV-L[1]) is observed in the month of March at the TIR site. During the southwest monsoon period of August (see table 5) 2018, a high forecast nRMSE (20.67% for TV-L[1]) and the lowest OLR (<210 W m^{-2}) is observed. The highest forecast error (23.46% for TV-L[1]) is found to be during the northeast monsoon period (see table 5) in December. However, a relatively high OLR of 265 W m^{-2} is observed in December. The daily averaged error in the 30 min ahead GHI forecast is found to be increasing gradually with the decrease in OLR, as shown in figure 9(b). The correlations are significant due to the low *p*-values. Days with high CI (>0.4) typically occur when the OLR is below 200 W m^{-2}. The exponential fit of CI against OLR shows the best correlation coefficient (0.72), see figure 10(b). On an average, TV-L[1] shows the best results for both the sites (see table 6).
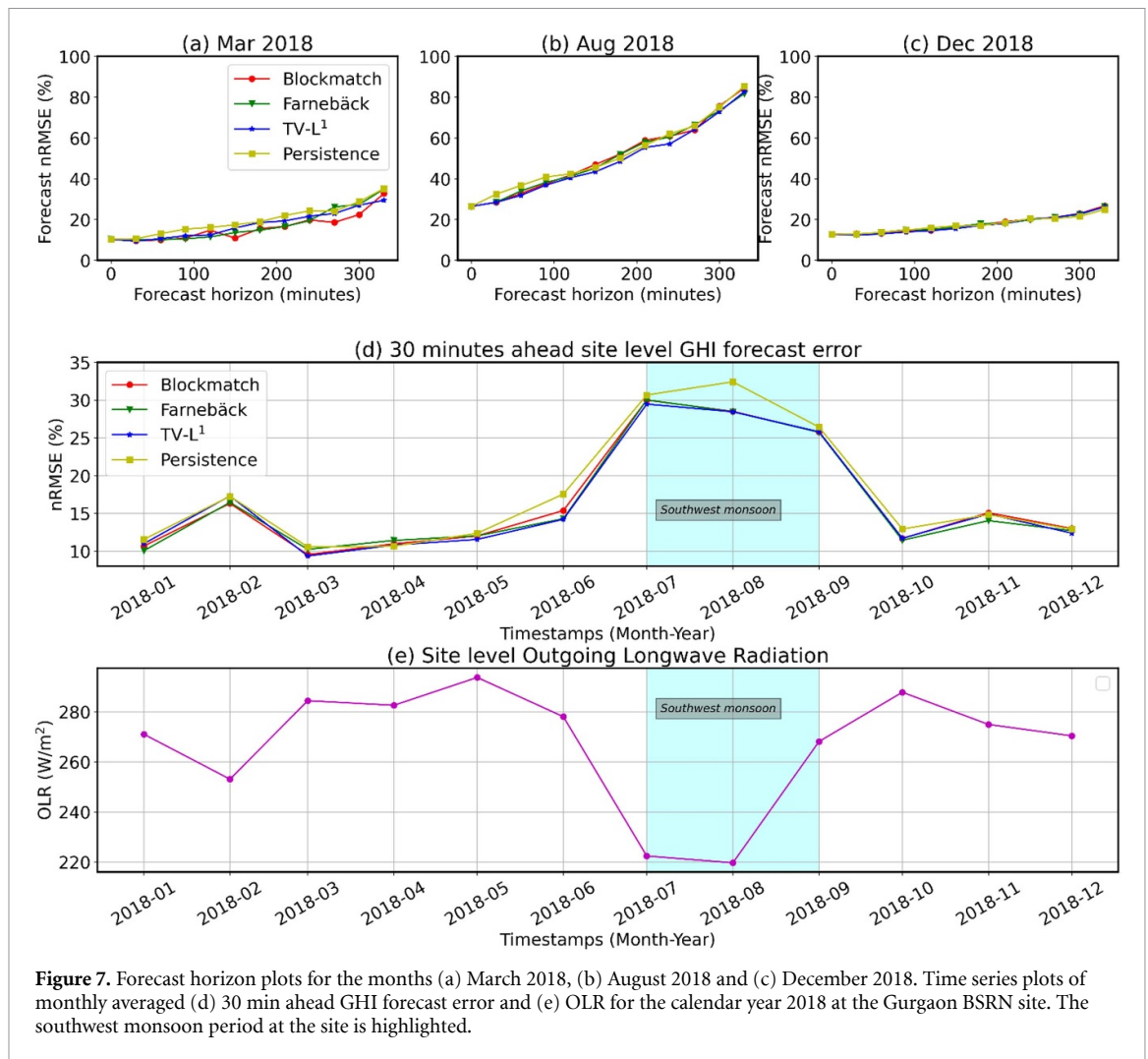
Figure 7. Forecast horizon plots for the months (a) March 2018, (b) August 2018 and (c) December 2018. Time series plots of monthly averaged (d) 30 min ahead GHI forecast error and (e) OLR for the calendar year 2018 at the Gurgaon BSRN site. The southwest monsoon period at the site is highlighted.

3.3. Evaluation of forecasted power

The percentage of time blocks with $Error_{PV}$ exceeding 10% is found to be maximum at the two sites for the convective period with low OLR (see figure 12). The highest benefit in using OF based methods over persistence is also observed during this convective period. Unlike the nRMSE metric for the GHI forecast, the percentage of erroneous blocks is not the highest in December at the TIR site. A similar pattern can be seen from the monthly GHI forecast nMAE plot for TIR (see figure 11). Note, that differences in the order of lines between figures 7 and 8 on the one hand and figures 11 and 12 on the other hand are due to the change in forecast horizon (30 min ahead and 90 min ahead).

4. Discussion

Out of the methods tested, TV-L^1 is found to outperform the others at both the section-wide and site level on an average. However, the inter-seasonal difference in forecast accuracy is far more significant than the inter-method difference in accuracy. The highest 30 min ahead section-wide CI forecast accuracy is observed in the month of March along with high section-wide OLR, indicating very little convection and low section-wide CI, signifying the prevalence of clear skies. The forecast accuracy then drops to a minimum in August accompanied by a sharp dip in OLR and a rise in CI, indicating a period of deep tropical convection. This is due to the fact that the southwest monsoon occurring in August (see table 5) affects a large part of the Indian subcontinent and parts of South Asia shown in the image section. The forecast accuracy rises to an intermediate value in December. This could be attributed to the relatively narrow area of influence of the northeast monsoon (Wonsick *et al* 2009, Misra and Bhardwaj 2019). In general, low forecast accuracy is expected for periods with heavy convection and high cloudiness. Huang *et al* (2018) found a similar relation between cloudiness and forecast accuracy with NWP forecast errors over the Australian landmass for 13 irradiance measurement stations. Our analysis demonstrates the contribution of convection towards low accuracy in satellite-based CI image forecasts. The increase in day-ahead GHI forecast error due to the difficulty in representing convection at the lower spatial resolution of an NWP, as reported in Gregory *et al* (2012), is also observed here in satellite based
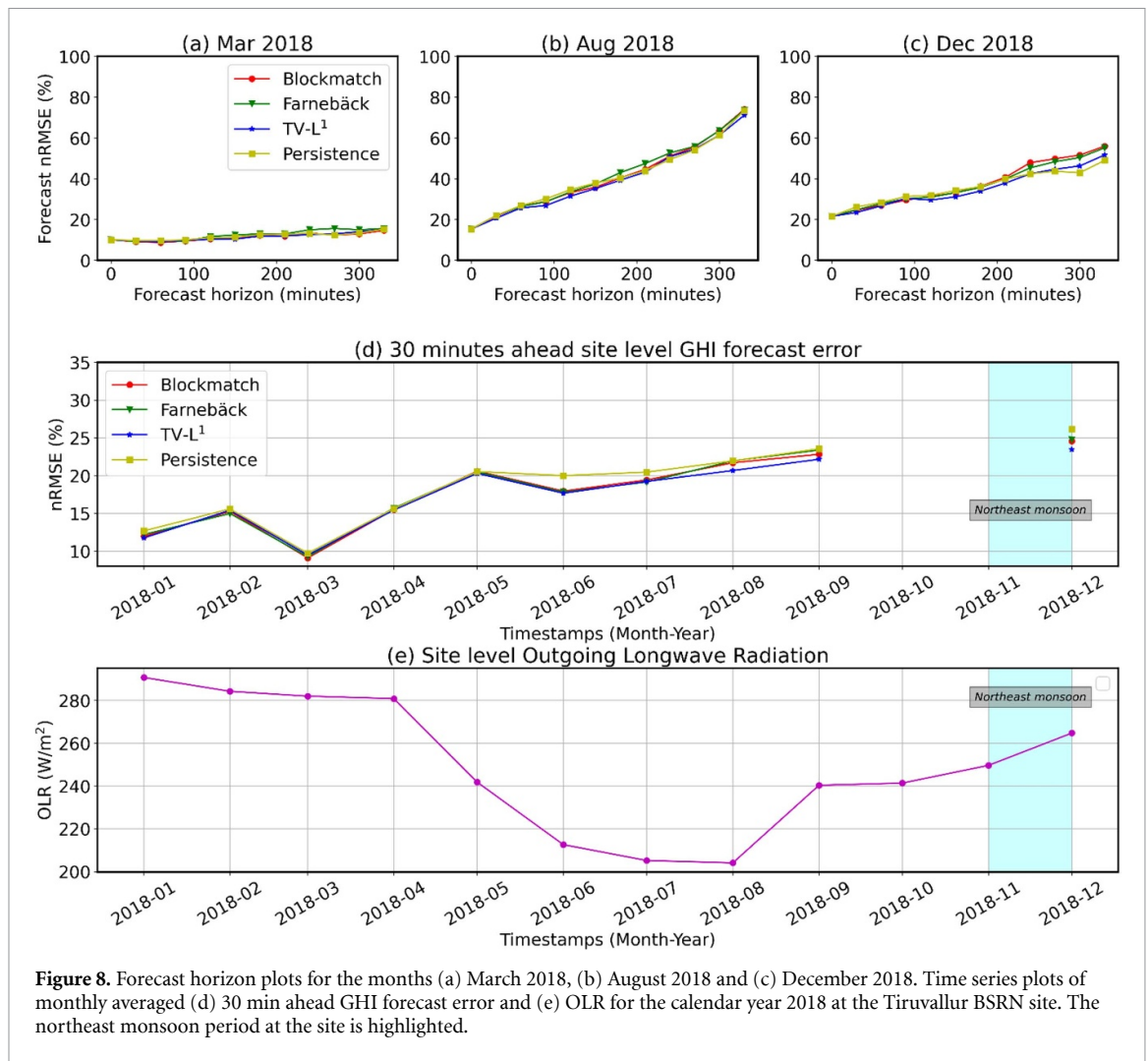
Figure 8. Forecast horizon plots for the months (a) March 2018, (b) August 2018 and (c) December 2018. Time series plots of monthly averaged (d) 30 min ahead GHI forecast error and (e) OLR for the calendar year 2018 at the Tiruvallur BSRN site. The northeast monsoon period at the site is highlighted.
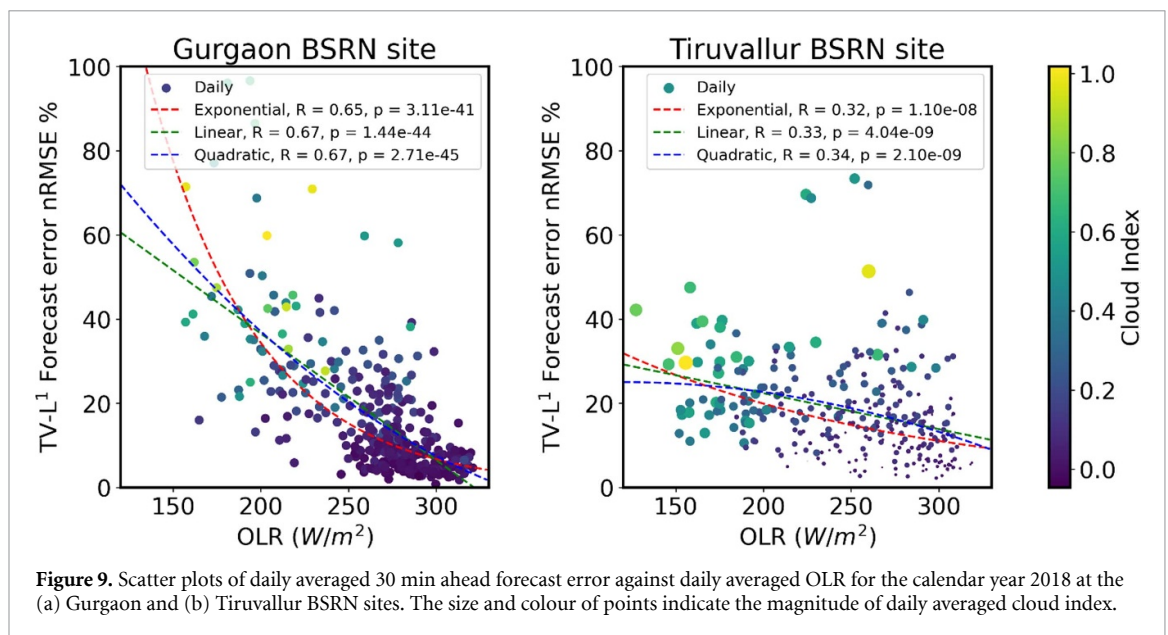
Figure 9. Scatter plots of daily averaged 30 min ahead forecast error against daily averaged OLR for the calendar year 2018 at the (a) Gurgaon and (b) Tiruvallur BSRN sites. The size and colour of points indicate the magnitude of daily averaged cloud index.

intra-day GHI forecasts with higher spatial resolution. However, a similar multi-year analysis of NWP and ground measured GHI data for a site in Helsinki, located in boreal climatic zone, revealed that there

is no seasonal difference in the relative error of predicted GHI (Tuononen *et al* 2019).

Seasonal variation of the 30 min ahead GHI forecast error at the GUR site is similar to that

Figure 10. Scatter plots of daily averaged cloud index against daily averaged OLR for the calendar year 2018 at the (a) Gurgaon and (b) Tiruvallur BSRN sites.
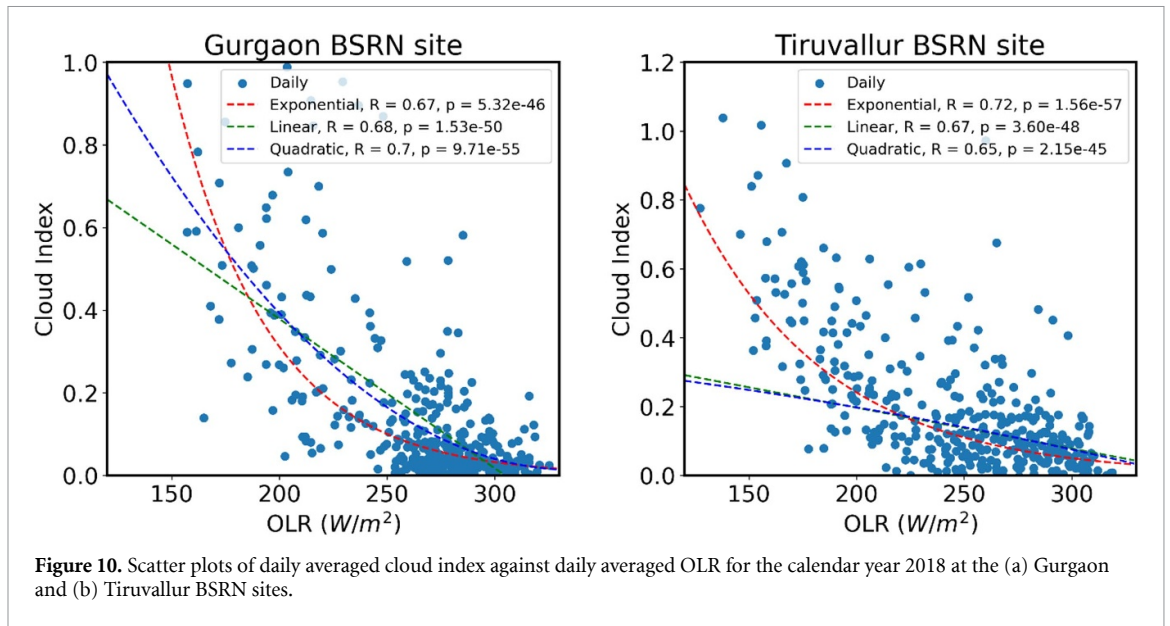
Table 6. Average performance of the 30 min ahead site-level GHI forecasts in 2018.

Method	Tiruvallur	Gurgaon
Blockmatch	18.39%	18.12%
Farnebäck	18.47%	17.93%
TV-L^1	18.07%	17.91%
Persistence	19.10%	19.00%

Figure 11. Time series plot of nMAE of 90 min ahead GHI forecast at (a) Gurgaon and (b) Tiruvallur.
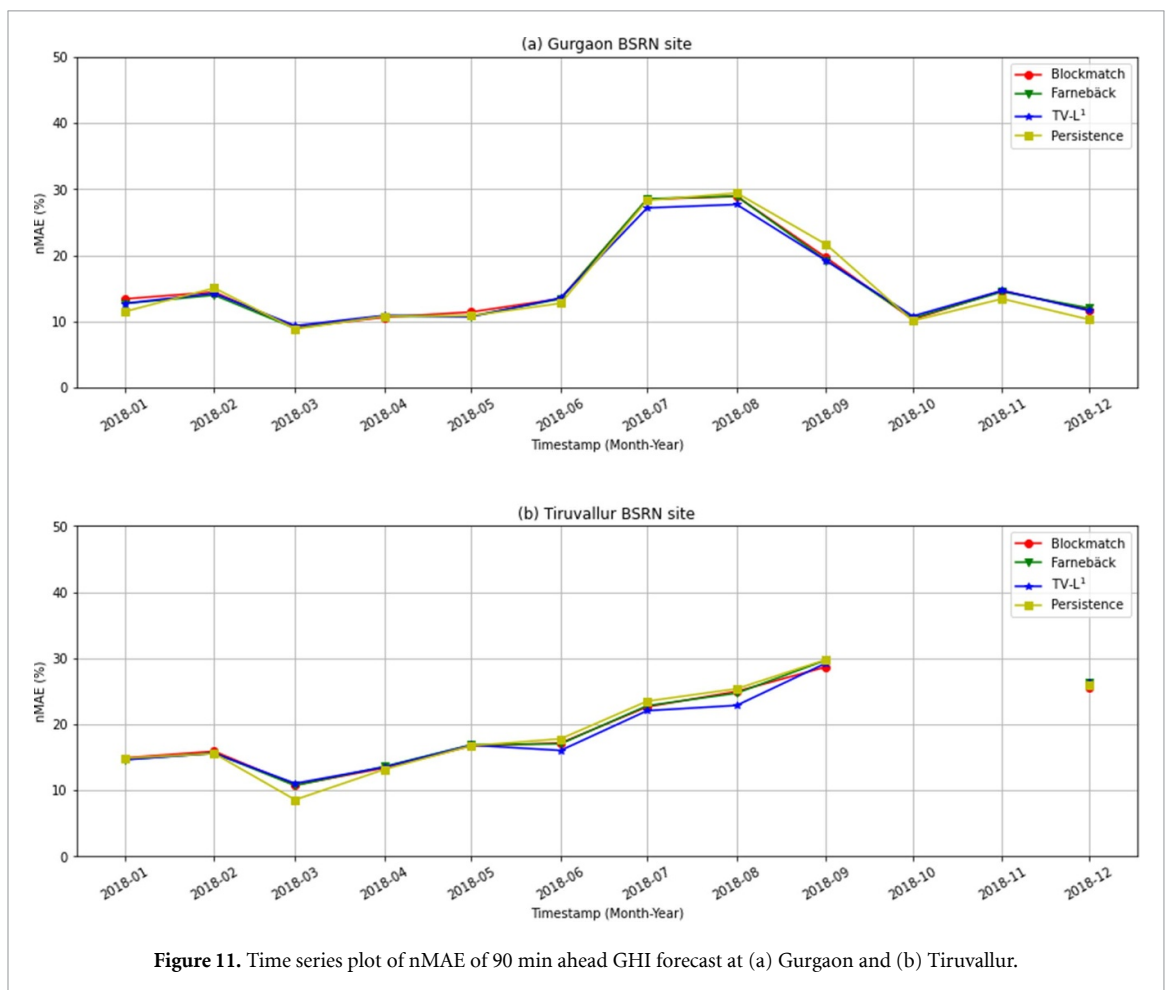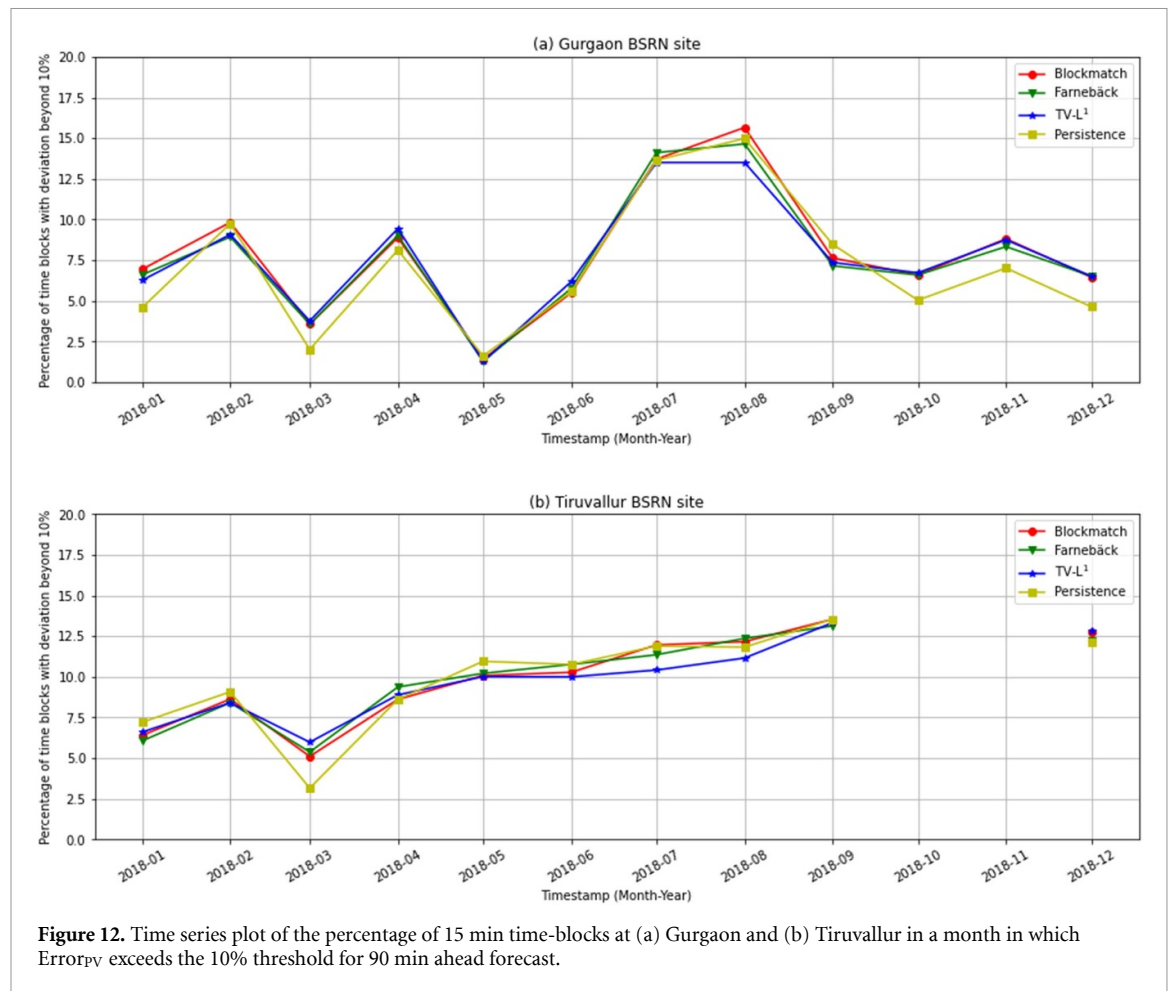
Figure 12. Time series plot of the percentage of 15 min time-blocks at (a) Gurgaon and (b) Tiruvallur in a month in which Error$_{PV}$ exceeds the 10% threshold for 90 min ahead forecast.

observed for the section-wide level CI forecast, except in December. The lowest average forecast error is observed in March, while the highest error is observed in August in the southwest monsoon period (see table 5). The error rises by a factor of 3 from March to August. This is accompanied by observations of very low OLR, as seen in the section-wide case. In December however, a low average forecast error is observed due to the location of the GUR site in a hot semi-arid climatic zone out of the influence of the northeast monsoon.

Higher average GHI forecast errors are observed at the TIR site. The lowest 30 min ahead GHI forecast error at the TIR site is also observed in March and subsequently the error climbs by a factor of 2 till August. The OLR drops to its lowest value in August. The forecast error further rises to reach the highest in the month of December, during the northeast monsoon period (see table 5). However, a relatively high OLR is observed in December compared to August. This could be attributed to the lower cloud top height observed during the northeast monsoon as noted in Amudha *et al* (2016) and Rajeevan *et al* (2012). Additionally, the northeast monsoon of December 2018 is also reported to have been deficient in terms of rainfall (https://mausam.imd.gov.in/chennai/mcdata/ne_monsoon_2018.pdf) and fits

well with the relatively high OLR observed. On an average, higher 30 min ahead GHI forecast errors are observed at TIR than at GUR. Our results show that it occurs due to the higher cloudiness at TIR, located in an Aw climatic zone, than GUR, located in a BSh climatic zone. Longer period with high cloudiness has also been reported for sites within the Aw zone than BSh in (An *et al* 2017, Bojanowski *et al* 2018). Majority of the cloudy period is observed at GUR during the seasonal southwest monsoon convection time. As a result, the forecast error increases sharply with the decrease in OLR. TIR has a longer cloudy period and not all the forecast error is due to deep convection with large cloud top height, as indicated by the relatively high OLR during northeast monsoon than in the southwest monsoon period at the site. Therefore, the increase in forecast error with OLR is more gradual.

By analysing the percentage of erroneous time blocks of forecasted 90 min ahead PV production for each method, we observed that the OF methods provided the greatest improvement against persistence during convective situations with low OLR. The number of erroneous blocks and nMAE in December at the TIR site is not the highest like nRMSE. This can be attributed to some large forecast errors, whose effects get amplified by the nRMSE metric.

5. Conclusion

By analysing 2 years of Meteosat-8 derived image sections of the Indian subcontinent with parts of South Asia and 1 year of ground measured GHI data from two BSRN sites located in India, we demonstrated the negative impact of the South Asian monsoon on CMV based forecast accuracy. Our findings suggest that a direct link can be established between convection and high forecast error. As discussed previously, the seasonality of forecast error is clearly dependent on the climatic zone (Gregory *et al* 2012, Huang *et al* 2018, Tuononen *et al* 2019). Our study provides added value by showing that the limitations observed in day-ahead NWP based prediction are also present in intra-day CMV based forecasts. It can also be seen from the results that the difference in accuracy between the block-match and the OF methods tested, is not significant in comparison to the inter-seasonal difference in forecast accuracy. The section-wide analysis provides a broader assessment than single site validation, and can provide insights to power system operators and policymakers on possible load-generation mismatch scenarios. We further examined the difference in the influence of convection on the forecast error at two sites located in different Köppen-Geiger climatic zones. Tropical savanna locations like TIR witness higher cloudiness, higher forecast errors and a more gradual increase in forecast error with the reduction in OLR than in semi-arid locations like GUR.

Tropical and sub-tropical regions, like the Indian subcontinent, receive a high amount of solar irradiance and are also undergoing a rapid increase in grid-connected solar PV capacity. However, the economic operation of such PV systems and the power system as a whole, is limited by the inherent inaccuracy in forecast. Our analysis provides timely information on the quality of intra-day forecast that can be expected. Viewing these results in the context of the deviation and imbalance settlement regulations provide stakeholders interested in large scale PV systems with an estimate of average risk or expected losses due to deviations. On the one hand, further development of models to better incorporate the effect of convection on GHI prediction is a major open question from energy-meteorology point of view. On the other hand, the knowledge that such a seasonal limitation of forecast accuracy exists would help grid operators and solar PV operators in better allocation of resource or bidding in the power exchange.

We can see that convection sets a limitation on the accuracy of satellite based CMV methods. One option could be to use images of higher spatio-temporal resolution such as those from the ground based all sky imagers, which would allow a finer demarcation of the advective and convective parts. However, it is still not feasible to model the formation and dissipation of clouds in these models. Using data from satellite and ground imagers as inputs into large eddy simulation is another way forward which has the possibility of being able to simulate cloud formation and dissipation. These topics are a part of the future planned work in our group. Furthermore, higher errors are expected during the convective period. In such situations, a probabilistic forecast could be more useful than a deterministic one.

Apart from convection, aerosols have a significant impact on satellite estimated or predicted GHI depending on the choice of clear sky model for the region considered here. However, this factor was ignored in the current study in order to focus the attention purely on cloudiness and convection.

Data availability statement

The data that support the findings of this study are available upon reasonable request from the authors.

ORCID iD

Arindam Roy ⓘ https://orcid.org/0000-0002-4866-571X

References

Aicardi D, Musé P and Alonso-Suárez R 2022 A comparison of satellite cloud motion vector techniques to forecast intra-day hourly solar global horizontal irradiation *Sol. Energy* **233** 46–60

Al-Amaren A, Ahmad M O and Swamy M N S 2021 A very fast edge map-based algorithm for accurate motion estimation *Signal Image Video Process.* **15** 1609–16

Amudha B, Raj Y E A and Asokan R 2016 Characteristics of movement of low level clouds associated with onset/wet spells of northeast monsoon of Indian sub-continent as derived from high resolution INSAT OLR data *MAUSAM* **67** 357–76

An N, Wang K, Zhou C and Pinker R T 2017 Observed variability of cloud frequency and cloud-base height within 3600 m above the surface over the contiguous United States *J. Clim.* **30** 3725–42

André M, Perez R, Soubdhan T, Schlemmer J, Calif R and Monjoly S 2019 Preliminary assessment of two spatio-temporal forecasting technics for hourly satellite-derived irradiance in a complex meteorological context *Sol. Energy* **177** 703–12

Bai J and Huang L 2018 Research on LK optical flow algorithm with Gaussian pyramid model based on OpenCV for single target tracking *IOP Conf. Ser.: Mater. Sci. Eng.* **435** 012052

Beck H E, Zimmermann N E, McVicar T R, Vergopolan N, Berg A and Wood E F 2018 Present and future Köppen-Geiger climate classification maps at 1-km resolution *Sci. Data* **5** 1–12

Bojanowski J S, Stöckli R, Duguay-Tetzlaff A, Finkensieper S and Hollmann R 2018 Performance assessment of the COMET cloud fractional cover climatology across Meteosat generations *Remote Sens.* **10** 804

Bright J M and Engerer N A 2019 Engerer2: global re-parameterisation, update, and validation of an irradiance separation model at different temporal resolutions *J. Renew. Sustain. Energy* **11** 033701

Bushair M T, Rani S I, Jangid B P, Sharma P, Kumar S, George J P and Das Gupta M 2021 Evaluation of the benefits of assimilation of Meteosat-8 observations in an NWP system over the Indian Ocean region *Meteorol. Atmos. Phys.* **133** 1555–76

Cheung K K W, Chooprateep S and Ma J 2015 Spatial and temporal patterns of solar absorption by clouds in Australia as revealed by exploratory factor analysis *Sol. Energy* **111** 53–67

Cros S, Badosa J, Szantaï A and Haeffelin M 2020 Reliability predictors for solar irradiance satellite-based forecast *Energies* **13** 5566

Cros S, Liandrat O, Sébastien N and Schmutz N 2014 Extracting cloud motion vectors from satellite images for solar power forecasting *IEEE Int. Geosci. Remote Sens. Symp.* pp 4123–6

Cros S, Sébastien N, Liandrat O and Schmutz N 2014a Cloud pattern prediction from geostationary meteorological satellite images for solar energy forecasting *Remote Sensing of Clouds and the Atmosphere XIX; and Optics in Atmospheric Propagation and Adaptive Systems XVII* vol 9242 p 924202

Das A 2017 Applicability of error limit in forecasting and scheduling of wind and solar power in India *ISGW 2017: Compendium of Technical Papers* ed R K Pillai *et al* (Singapore: Springer Nature) p 263

Davy R J and Troccoli A 2011 Interannual variability of solar energy generation in Australia *Sol. Energy* **86** 3554–60

Driemel A *et al* 2018 Baseline Surface Radiation Network (BSRN): structure and data description (1992–2017) *Earth Syst. Sci. Data* **10** 1491–501

Dumortier D 1995 Modelling global and diffuse horizontal irradiances under cloudless skies with different turbidities *Final Report JOU2-CT92-0144, Daylight II Technical Report* (Vaulx-enVelin: Ecole Nationale des Travaux Publics de l'État)

Gadgil S 2003 The Indian monsoon and its variability *Annu. Rev. Earth Planet. Sci.* **31** 429–67

Gallucci D *et al* 2018 Nowcasting surface solar irradiance with AMESIS via motion vector fields of MSG-SEVIRI data *Remote Sens.* **10** 845

Geiss S, Scheck L, de Lozar A and Weissmann M 2021 Understanding the model representation of clouds based on visible and infrared satellite observations *Atmos. Chem. Phys.* **21** 12273–90

Ghanekar S P, Puranik P V and Mujumdar V R 2010 Application of satellite-derived OLR data in the prediction of the onset of Indian summer monsoon *Theor. Appl. Climatol.* **99** 457–68

Gregory P A, Rikus L J and Kepert J D 2012 Testing and diagnosing the ability of the Bureau of Meteorology's numerical weather prediction systems to support prediction of solar energy production *J. Appl. Meteorol. Climatol.* **51** 1577–601

Hammer A, Heinemann D, Lorenz E and Lückehe B 1999 Short-term forecasting of solar radiation: a statistical approach using satellite data *Sol. Energy* **67** 139–50

Hammer A, Kühnert J, Weinreich K and Lorenz E 2015 Short-term forecasting of surface solar irradiance based on Meteosat-SEVIRI data using a nighttime cloud index *Remote Sens.* **7** 9070–90

Huang J, Rikus L J, Qin Y and Katzfey J 2018 Assessing model performance of daily solar irradiance forecasts over Australia *Sol. Energy* **176** 615–26

Hutt A *et al* 2020 Assimilation of SEVIRI water vapor channels with an ensemble Kalman filter on the convective scale *Front. Earth Sci.* **8** 70

Jiang N and Zhu C 2020 Tropical Pacific cold tongue mode triggered by enhanced warm pool convection due to global warming *Environ. Res. Lett.* **15** 054015

Kallio-Myers V, Riihelä A, Lahtinen P and Lindfors A 2020 Global horizontal irradiance forecast for Finland based on geostationary weather satellite data *Sol. Energy* **198** 68–80

Kim C K, Kim H-G, Kang Y-H and Yun C-Y 2017 Toward improved solar irradiance forecasts: comparison of the global horizontal irradiances derived from the COMS satellite imagery over the Korean Peninsula *Pure Appl. Geophys.* **174** 2773–92

Kumar A, Gomathinayagam S, Giridhar G, Mitra I, Vashistha R, Meyer R, Schwandt M and Chhatbar K 2014 Field experiences with the operation of solar radiation resource assessment stations in India *Energy Proc.* **49** 2351–61

Kumar A, Mittal S and Ghosal A 2021 Impact on Indian power grid due to large scale integration of solar energy by 2022 *Water Energy Int.* **64** 49–55

Lara-Fanego V, Ruiz-Arias J A, Pozo-Vázquez D, Santos-Alamillos F J and Tovar-Pescador J 2012 Evaluation of the WRF model solar irradiance forecasts in Andalusia (Southern Spain) *Sol. Energy* **86** 2200–17

Lee J A, Haupt S E, Jiménez P A, Rogers M A, Miller S D and McCandless T C 2017 Solar irradiance nowcasting case studies near Sacramento *J. Appl. Meteorol. Climatol.* **56** 85–108

Li Y, Chen X and Yang M 2019 Optical flow based solar irradiance forecasting in satellite images *IEEE Int. Conf. Real-time Comput. Robot (RCAR)* (*Russia, 4–9 August*) pp 442–7

Liebmann B and Smith C A 1996 Description of a complete (interpolated) outgoing longwave radiation dataset *Bull. Am. Meteorol.* **77** 1275–7 www.jstor.org/stable/26233278

Lorenz E, Hammer A and Heinemann D 2004 Short term forecasting of solar radiation based on satellite data *Conf. Proc. EUROSUN 2004* (*Germany, 20–23 June*) p 1

Malik A *et al* 2020 Reducing stranded assets through early action in the Indian power sector *Environ. Res. Lett.* **15** 094091

Mao J and Wu G 2007 Interannual variability in the onset of the summer monsoon over the Eastern Bay of Bengal *Theor. Appl. Climatol.* **89** 155–70

Mejia J F, Giordano M and Wilcox E 2018 Conditional summertime day-ahead solar irradiance forecast *Sol. Energy* **163** 610–22

Midhuna T M and Dimri A P 2019 Impact of arctic oscillation on Indian winter monsoon *Meteorol. Atmos. Phys.* **131** 1157–67

Misra V and Bhardwaj A 2019 Defining the northeast monsoon of India *Mon. Weather Rev.* **147** 791–807

Oh M, Kim C K, Kim B, Yun C, Kang Y and Kim H 2021 Spatiotemporal optimization for short-term solar forecasting based on satellite imagery *Energies* **14** 2216

Ohtake H, Fonseca J G S, Takashima T, Oozeki T, Shimose K-I and Yamada Y 2015 Regional and seasonal characteristics of global horizontal irradiance forecasts obtained from the Japan Meteorological Agency mesoscale model *Sol. Energy* **116** 83–99

Ohtake H, Shimose K-I, Fonesca J G S, Takashima T, Oozeki T and Yamada Y 2013 Accuracy of the solar irradiance forecasts of the Japan Meteorological Agency mesoscale model for the Kanto region, Japan *Sol. Energy* **98** 138–52

Pérez J S, Meinhardt-Llopis E and Facciolo G 2013 TV-L^1 optical flow estimation *Image Process. Line* **3** 137–50

Perez R, Ineichen P, Seals R, Michalsky J and Stewart R 1990 Modeling daylight availability and irradiance components from direct and global irradiance *Sol. Energy* **44** 271–89

Poobathy D and Chezian R M 2014 Edge detection operators: peak signal to noise ratio based comparison *Int. J. Image Graph. Signal Process.* **10** 55–61

Prasad A A and Kay M 2021 Prediction of solar power using near-real time satellite data *Energies* **14** 5865

Rajeevan M, Unnikrishnan C K, Bhate J, Kumar N K and Sreekala P P 2012 Northeast monsoon over India: variability and prediction *Meteorol. Appl.* **19** 226–36

Sharma A, Mitra A, Vasan V and Govindarajan R 2021
Spatio-temporal relationships between rainfall and
convective clouds during Indian monsoon through a
discrete lens *Int. J. Climatol.* **41** 1351–68

Sikka D R, Paul D K, Deshpande V R, Mujumdar V R and
Puranik P V 1986 Sub-seasonal scale fluctuations of the
ITCZ over the Indo-Pacific region during the summer
monsoon season. Part I: features over the Indian
region *Proc. Indian Acad. Sci. Earth Planet. Sci.*
95 47–73

Su H, Wu L, Zhai C, Jiang J H, Neelin D and Yung Y L 2020
Observed tightening of tropical ascent in recent decades and
linkage to regional precipitation changes *Geophys. Res. Lett.*
47 e2019GL085809

Tuononen M, O' Connor E J and Sinclair V A 2019 Evaluating
solar radiation forecast uncertainty *Atmos. Chem. Phys.*
19 1985–2000

Turner A G and Annamalai H 2012 Climate change and the
South Asian summer monsoon *Nat. Clim. Change*
2 587–95

Urbich I, Bendix J and Müller R 2018 A novel approach for the
short-term forecast of the effective cloud albedo *Remote
Sens.* **10** 955

Urbich I, Bendix J and Müller R 2019 The seamless solar radiation
(SESORA) forecast for solar surface irradiance—method
and validation *Remote Sens.* **11** 2576

Wonsick M M, Pinker R T and Govaerts Y 2009 Cloud variability
over the Indian monsoon region as observed from satellites
J. Appl. Meteorol. Climatol. **48** 1803–21

Yamazaki K and Nakamura T 2021 The stratospheric QBO affects
Antarctic sea ice through the tropical convection in early
austral winter *Polar Sci.* **28** 100674

Yang L, Gao X, Hua J, Wu P, Li Z and Jia D 2020 Very short-term
surface solar irradiance forecasting based on FengYun-4
geostationary satellite *Sensors* **20** 2606

Yang Y, Gao G, Li L I, Jia J and Jiang J 2019 Nowcasting of surface
solar irradiance using FengYun-4 satellite observations over
China *Remote Sens.* **11** 1984

Zach C, Pock T and Bischof H 2007 A duality based approach for
realtime TV-L^1 optical flow *Joint Pattern Recognition
Symp.* (*Germany, 12–14 September*) (Springer)
pp 214–23

Zhai H, Zhang H, Zhang L and Li P 2018 Cloud/shadow detection
based on spectral indices for multi/hyperspectral optical
remote sensing imagery *ISPRS J. Photogramm. Remote Sens.*
144 235–25